Journal of Nuclear Materials 389 (2009) 155–159

Contents lists available at ScienceDirect

Journal of Nuclear Materials

journal homepage: www.elsevier.com/locate/jnucmat

Thermophysical properties of $(U,Y)O_2$

Hiromichi Gima, Ken. Kurosaki *, Jun Adachi, Masahito Katayama, Hiroaki Muta, Masayoshi Uno, Shinsuke Yamanaka

Graduate School of Engineering, Osaka University, 2-1 Yamadaoka, Suita Osaka 565-0871, Japan

A B S T R A C T

We prepared polycrystalline pellets of $(U,Y)O_2$, containing $YO_{1.5}$ up to 11 mol.%. We performed indentation tests on the pellets, and evaluated the Young's modulus and hardness. We measured the heat capacity and the thermal diffusivity, and evaluated the thermal conductivity. We succeeded in evaluating the effect of Y content on the thermophysical properties of $(U,Y)O_2$. We revealed that the Young's modulus, hardness, and thermal conductivity of $(U,Y)O_2$ decreased with increasing the Y content.

1. Introduction

Uranium dioxide (UO_2) fuels doped with a small amount of erbium oxide ($ErO_{1.5}$) are being studied as next-generation fuels for light-water reactors. When utilizing $(U,Er)O_2$ as nuclear fuels, it is very important to understand the crystallographic nature, mechanical properties, thermal properties, and thermophysical properties, to evaluate the fuel safety and performance. However, these properties of $(U,Er)O_2$ have been scarcely reported. Therefore, we are now studying the thermophysical properties of $(U,Er)O_2$ and investigating the effect of $ErO_{1.5}$ addition on the properties of UO_2 [1].

In the present study, we paid attention to $(U,Y)O_2$ because Y^{3+} have similar ionic radius (0.102 nm) with Er^{3+} (0.100 nm) [2] but the atomic weight of Y (88.91) differs substantially from Er (167.3). By collecting the thermophysical properties of $(U,Y)O_2$ and by comparing them with those of $(U,Er)O_2$, we can discuss the results from the viewpoint of fundamental aspects. In addition, the present study would also be useful in evaluating the performance of irradiated UO_2 fuels, because Y is known as a major fission product which dissolves in the UO_2 matrix phase.

2. Experiment

We prepared six compositions of the samples: $(U_{1-x}Y_x)O_2$ (x = 0, 0.01, 0.03, 0.05, 0.1, and 0.11). Appropriate amounts of UO_2 and Y_2O_3 powders were mixed and pressed into pellets, followed by reacting at 1773 K under a reducing atmosphere. The obtained intermediates were crushed to powders and pressed into pellets under 150 MPa, followed by sintering at 1873 K in a H_2–Ar gas flow atmosphere for 5 h. Finally, the pellets were sintered again at 1373 K in a desired reducing atmosphere for 40 h to fix the oxygen to metal (O/M) ratio to be 2.00.

To examine the sample purity and determine the lattice parameter, the X-ray diffraction (XRD) data were collected on a diffractometer on (RINT2000 Rigaku) with Cu Kα radiation in air at room temperature. The sample microstructure was observed by using a scanning electron microscope (SEM) and electron backscatter diffraction (EBSD). The chemical composition of the samples was determined using an energy-dispersive X-ray (EDX) analysis in vacuum at room temperature.

Hardness (H) and Young's modulus (E) were determined with the indentation tests using a dynamic ultra-microhardness tester at room temperature. The maximum load was chosen to be 3, 5, 7, 10, 50, 100, 500, and 1000 mN under a loading/unloading time of 15 s and a maximum load retention time of 2 s. The Vickers hardness was also measured using a Vickers hardness tester at room temperature under a maximum load of 490 mN and 9800 mN.

Thermal conductivity (κ) was calculated from heat capacity (C_P), thermal diffusivity (α), and density (d) using the following relationship:

$$\kappa = \alpha C_P d. \tag{1}$$

The heat capacity was measured by a differential scanning calorimeter, in the temperature range from room temperature to 1273 K in an Ar-flow atmosphere. The thermal diffusivity was measured by a laser flash technique in vacuum from 323 to 1473 K, and the density was calculated from the sample's weight and dimensions at room temperature.

3. Results and discussion

Fig. 1 shows the XRD patterns of the $(U_{1-x}Y_x)O_2$ (x = 0, 0.05, and 0.1) samples, together with the peak positions obtained from the JCPDS cards [3]. In all XRD patterns, there were no peaks derived

* Corresponding author. Tel.: +81 6 6879 7905; fax: +81 6 6879 7889.
E-mail address: kurosaki@see.eng.osaka-u.ac.jp (K. Kurosaki).

0022-3115/$ - see front matter © 2009 Elsevier B.V. All rights reserved.
doi:10.1016/j.jnucmat.2009.01.021

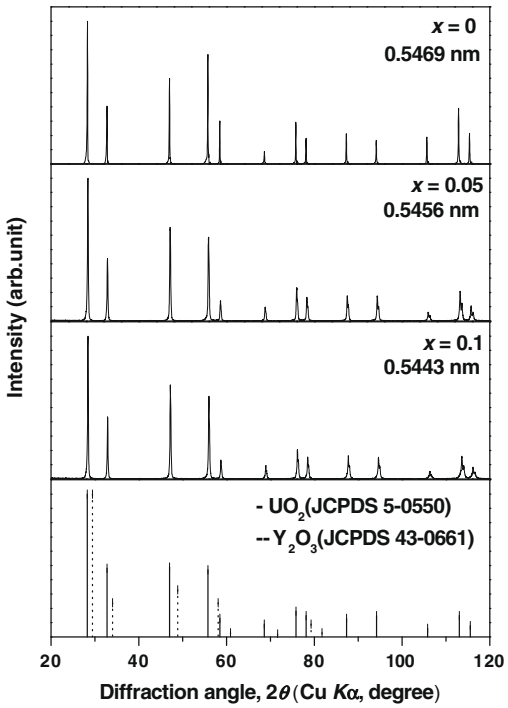

Fig. 1. XRD patterns of $(U_{1-x}Y_x)O_2$ ($x = 0$, 0.05, and 0.1), together with the peak positions obtained from the JCPDS cards [3].

from impurities; a single phase with a fluorite structure was detected. In addition, the high angle diffraction peaks were well spilt into $K\alpha_1$ and $K\alpha_2$, indicating the complete solid solution formation. The cubic lattice parameter was calculated from the XRD pattern, as also shown in Fig. 1. The lattice parameter of $(U,Y)O_2$ decreased linearly with increasing the Y content. We obtained the following equation describing the effect of Y content on the lattice parameters of $(U_{1-x}Y_x)O_2$:

$$a(\mathrm{nm}) = 0.5468 - 0.0253x \quad (0 \leqslant x \leqslant 0.11). \tag{2}$$

The decreasing rate of the lattice parameters of $(U,Y)O_2$ with the Y content was very similar to those of $(U,Er)O_2$ [1], which was most likely due to the similar ionic radius of Y^{3+} and Er^{3+}.

From the SEM and EDX analyses, we confirmed that there were no segregations of particular elements throughout the surface of all samples. In addition, we also confirmed that the chemical compositions of the products did not deviate a lot from the starting compositions.

The inverse pole figure (IPF) mapping images of $(U_{1-x}Y_x)O_2$ ($x = 0$, 0.05, and 0.1) samples obtained from the EBSD analysis are shown in Fig. 2(a), (b), and (c), respectively, in which color of each grain corresponds to the crystal orientation. It was confirmed that the distributions of grains alignment are completely random in all samples, whereas the grain size appeared to decrease with the Y content. The average grain sizes estimated from the IPF mapping images are shown in Fig. 2(d). The average grain size decreased rapidly with including the Y content, even only 1 at.% Y-adding. The sample bulk densities are plotted in Fig. 2(e), as a function of the Y content. The density decreased with increasing

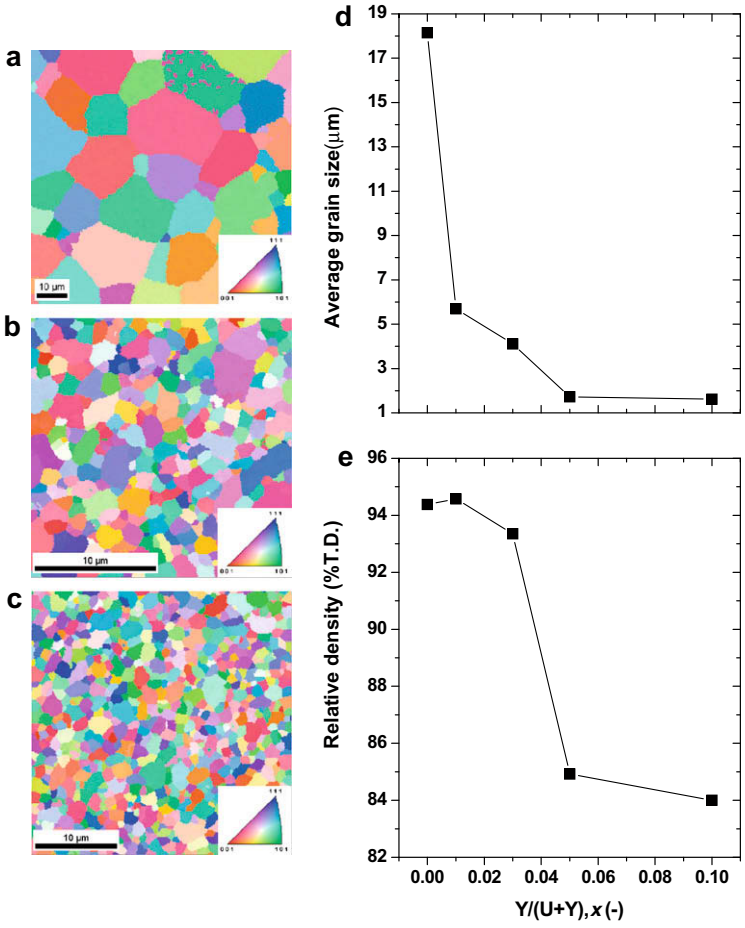

Fig. 2. IPF mapping images of the samples: (a) $x = 0$, (b) $x = 0.05$, and (c) $x = 0.1$ for $(U_{1-x}Y_x)O_2$. (d) Average grain size of the samples, as a function of the Y content. (e) Bulk density of the samples, as a function of the Y content.

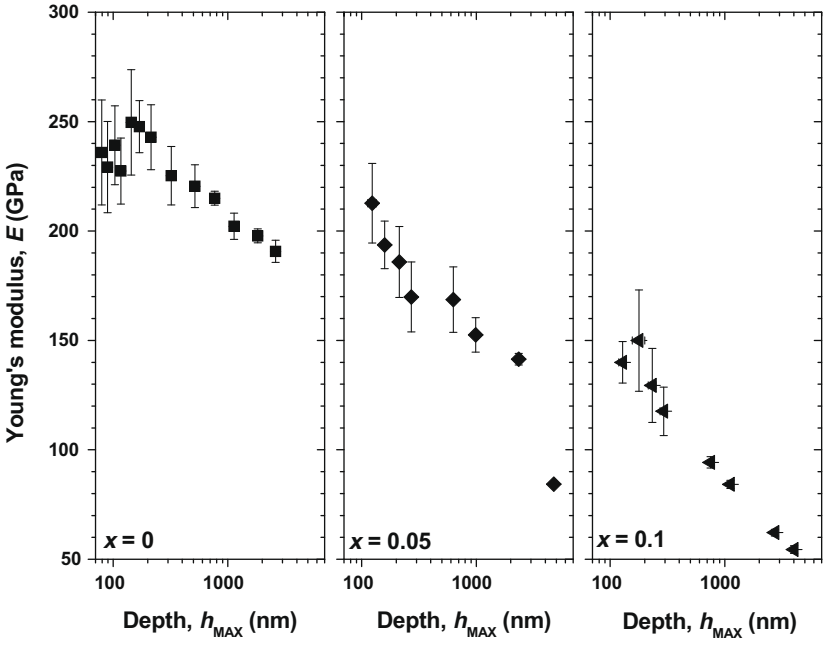

Fig. 3. Relationship between the Young's modulus and the indentation depth for $(U_{1-x}Y_x)O_2$ ($x = 0$, 0.05, and 0.1).

the Y content, like the grain size. In the low Y content region below 1 at.%, we were able to obtain high density pellets with approximately 95% of the theoretical density (%T.D.), whereas in the medium Y content regions, for example, 3 at.%, the density was around 90%T.D. and in the higher Y regions, i.e., 5 and 10 at.%, the densities were low as around 84%T.D. These low densities would be closely related with the grain size. The present study revealed that a small amount of Y addition to UO_2 even only a few percent encumbered the grain growth and consequently drastically degenerated the sintering behavior. The same tendency has been observed in $(U,Er)O_2$ [1,4].

The Young's moduli (E) of $(U_{1-x}Y_x)O_2$ ($x = 0$, 0.05, and 0.1) determined through the indentation tests are shown in Fig. 3, as a function of the indentation depth. The Young's modulus of all samples was independent of the indentation depth in the low depth regions, whereas it rapidly decreased with increasing the indentation depth in the high depth regions. These phenomena could be accounted for that the elastic deformation zone might reach at the grain boundary in the high depth region and the expansion of the elastic deformation zone might be promoted by the grain boundary. In the present study, the intrinsic Young's modulus (E_i) of the sample was estimated as an average value obtained in the low depth regions, in which the Young's modulus was not influenced by sample's microstructures. In Fig. 5(a), the E_i values of $(U,Y)O_2$ are plotted as a function of the Y content. It can be observed that the E_i of UO_2 obtained in the present study was well consistent with the literature data [5–10]. In addition, the E_i of $(U,Y)O_2$ decreased with the Y content. By using the data up to 5 at.%-Y added samples, we obtained the following equation describing the E_i of $(U_{1-x}Y_x)O_2$:

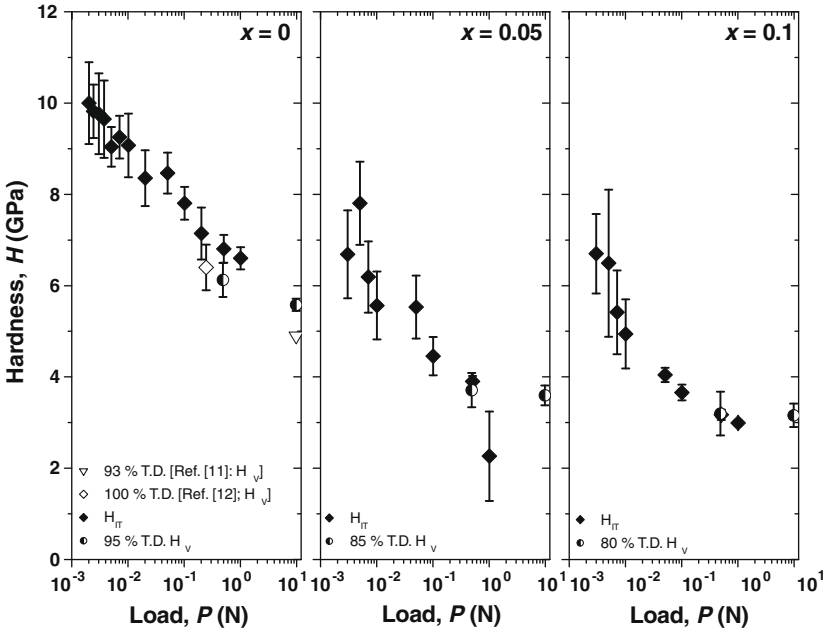

Fig. 4. Relationship between the hardness and the indentation load for $(U_{1-x}Y_x)O_2$ ($x = 0$, 0.05, and 0.1), together with the literature data of UO_2 [11,12].

$$E_i(\mathrm{GPa}) = 236 - 440x \quad (0 \leqslant x \leqslant 0.05). \tag{3}$$

Since the sample bulk density of the $x = 0.1$ sample was too low to perform the indentation test with no influences of the pores and grain boundaries even at the low depth regions, the E_i of the $x = 0.1$ sample was lower than the line of Eq. (3).

Fig. 4 shows the load dependence of the indentation hardness (H_{it}) and Vickers hardness (H_V) of $(U,Y)O_2$, together with the literature data [11,12]. Both the H_{it} and H_V decrease with the load increasing. In order to eradicate the influence of the indentation load on the hardness, we estimated the hardness at the adequate large depth (H_0) from the load-displacement curves, based on the Nix and Gao model [13]. Fig. 5(b) shows the H_0 of $(U,Y)O_2$, as a function of the Y content. It can be confirmed that the H_0 decreased with the Y content. We obtained the following equation describing the H_0 of $(U_{1-x}Y_x)O_2$:

$$H_0(\mathrm{GPa}) = 7.25 - 49.3x \quad (0 \leqslant x \leqslant 0.10). \tag{4}$$

The heat capacity (C_P) data of $(U,Y)O_2$ were similar in the investigated composition range (not shown). Therefore, we used the C_P data of UO_2 in calculating the thermal conductivities of $(U,Y)O_2$.

The temperature dependence of the thermal conductivity (κ) of $(U,Y)O_2$ is shown in Fig. 6, together with the literature data of UO_2 [8]. These values were corrected to the values for fully dense pellets with 100%T.D. by using the following equation [14]:

$$\kappa_0 = \kappa_P \frac{1 + \beta P}{1 - P}, \tag{5}$$

where κ_P is the measured thermal conductivity with certain porosities, κ_0 is the corrected thermal conductivity for fully dense pellets, P is the porosity, and β is a constant (= 0.5). The κ of

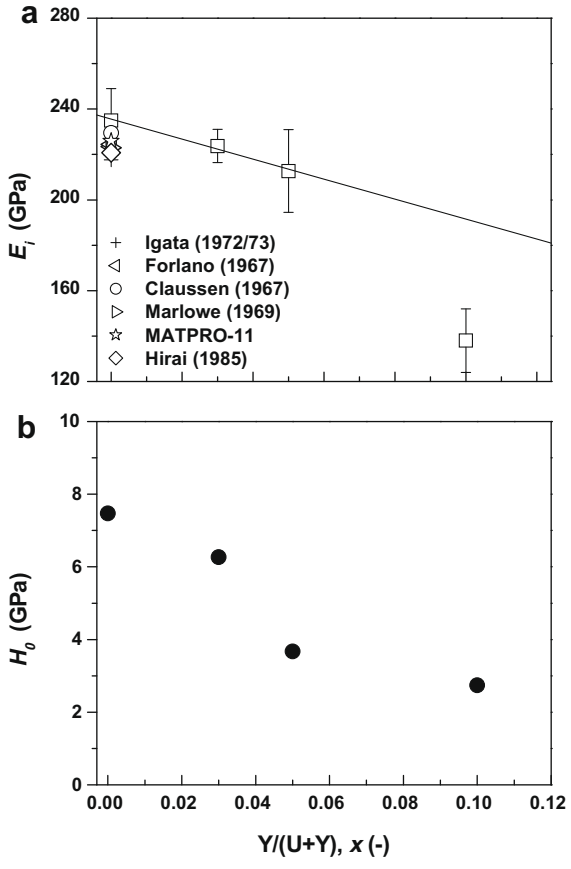

Fig. 5. (a) Intrinsic Young's modulus (E_i) and (b) the hardness at the adequate large depth (H_0) of $(U,Y)O_2$, as a function of the Y content. (a) The literature data for UO_2 [5–10] are shown for comparison.

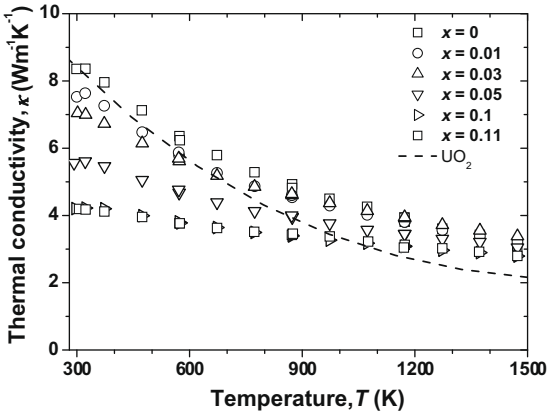

Fig. 6. Temperature dependence of the thermal conductivities of $(U,Y)O_2$, together with the literature data of UO_2 [8].

$(U,Y)O_2$ decreased with the Y content, indicating that Y in the UO_2 cell acted as centers of phonon scattering. Fig. 7 shows the thermal conductivities of $(U,Y)O_2$ and $(U,Er)O_2$ [1] at 1373 K and 773 K, as a function of the Y or Er content. From these figures, we confirmed that the reduction rate of κ of $(U,Y)O_2$ was slightly larger than that of $(U,Er)O_2$. This was due to the large difference of the atomic weight between Y and U compared with that between Er and U. We could obtain the following empirical equation describing the κ of $(U,Y)O_2$:

$$\kappa(\mathrm{Wm^{-1}K^{-1}}) = \frac{1}{3.60 \times 10^{-2} + 1.91x + (1.58 - 5.66x) \times 10^{-4}T} \times (0 \leqslant x \leqslant 0.11, 298K < T < 1473K). \tag{6}$$

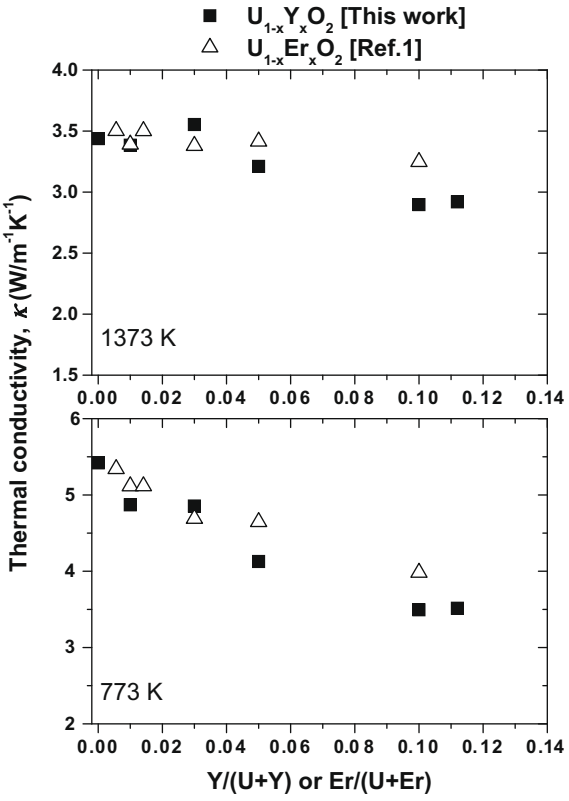

Fig. 7. Thermal conductivities at 773 K and 1373 K vs. Y or Er content in $(U,Y)O_2$ or $(U,Er)O_2$ [1].

4. Summary

We prepared polycrystalline pellets of $(U_{1-x}Y_x)O_2$ $(0 \leqslant x \leqslant 0.11)$ and measured their thermophysical properties. We succeeded in evaluating the effect of Y addition on the lattice parameter, Young's modulus, hardness, and thermal conductivity of $(U,Y)O_2$, as described as Eqs. (2)–(4), and Eq. (6), respectively. The results obtained in the present study would be useful in evaluating the effect of adding elements on the thermophysical properties of UO_2.

References

[1] S. Yamanaka, K. Kurosaki, M. Katayama, J. Adachi, M. Uno, T. Kuroishi, M. Yamasaki, J. Nucl. Mater. 389 (2009) 115.
[2] R.D. Shannon, Acta Crystallogr. A3 2 (5) (1976) 751.
[3] JCPDS 5-550 (UO_2), JCPDS 43-0661 (Y_2O_3).
[4] H.S. Kim, M.S. Yang, D.S. Sohn, JAERI-conference 96-006, in: Proceedings of the Workshop on Manufacturing Technology and Process for Reactor Fuels, vol. 1995, 1996, pp. 65–91.
[5] R.J. Forlano, A.W. Allen, R.J. Beals, J. Am. Ceram. Soc. 50 (1967) 93.
[6] V.N. Claussen, Berichte der Deutschen Keramischen Gesellschaft, vol. 44, 1967, p. 267.
[7] M.O. Marlowe, A.I. Kaznoff, Ceram. Nucl. Fuels Proc. Int. Symp. (1969) 90–99.
[8] D.L. Hagrman, G.A. Reyman, NUREG/CR-0497, TREE-1280, Rev. 3, 1979.
[9] N. Igata, K. Domoto, J. Nucl. Mater. 45 (1972/73) 317.
[10] M. Hirai, in: Proceedings of Fall Meetings of the Atomic Energy Society of Japan, Sendai, Japan, F58, 2–5 October 1985.
[11] A.K. Sengupta, C.B. Basak, T. Jarvis, R.K. Bhagat, V.D. Pandey, S. Majumdar, J. Nucl. Mater. 325 (2004) 141.
[12] K. Yamada, S. Yamanaka, M. Katsura, J. Alloys Compd. 271–273 (1998) 697.
[13] W.D. Nix, H. Gao, J. Mech. Phys. Solids 46 (1998) 411.
[14] A. Biancheria, Trans. Am. Nucl. Soc. 9 (1966) 15.